HIGH POWER LASER
SCIENCE AND ENGINEERING

RESEARCH ARTICLE

Specifications and control of spatial frequency errors of components in two-beam laser static holographic exposure for pulse compression grating fabrication

Chen Hu[1,2,3], Songlin Wan[1,2], Guochang Jiang[1,2], Haojin Gu[1,2], Yibin Zhang[2], Yunxia Jin[2],
Shijie Liu[1,2,3,5], Chengqiang Zhao[2], Hongchao Cao[2], Chaoyang Wei[1,2,3], and Jianda Shao[1,2,3,4,5]

[1] *Precision Optical Manufacturing and Testing Center, Shanghai Institute of Optics and Fine Mechanics, Chinese Academy of Sciences (CAS), Shanghai, China*

[2] *Key Laboratory for High Power Laser Material of Chinese Academy of Sciences, Shanghai Institute of Optics and Fine Mechanics, CAS, Shanghai, China*

[3] *Center of Materials Science and Optoelectronics Engineering, University of Chinese Academy of Sciences, Beijing, China*

[4] *Hangzhou Institute for Advanced Study, University of Chinese Academy of Sciences, Hangzhou, China*

[5] *China-Russian Belt and Road Joint Laboratory on Laser Science, Shanghai, China*

(Received 11 June 2023; revised 14 September 2023; accepted 22 September 2023)

Abstract

The large-aperture pulse compression grating (PCG) is a critical component in generating an ultra-high-intensity, ultra-short-pulse laser; however, the size of the PCG manufactured by transmission holographic exposure is limited to large-scale high-quality materials. The reflective method is a potential way for solving the size limitation, but there is still no successful precedent due to the lack of scientific specifications and advanced processing technology of exposure mirrors. In this paper, an analytical model is developed to clarify the specifications of components, and advanced processing technology is adopted to control the spatial frequency errors. Hereafter, we have successfully fabricated a multilayer dielectric grating of 200 mm $\times$ 150 mm by using an off-axis reflective exposure system with $\Phi 300$ mm. This demonstration proves that PCGs can be manufactured by using the reflection holographic exposure method and shows the potential for manufacturing the meter-level gratings used in 100 petawatt class high-power lasers.

Keywords: high-power laser; off-axis reflective exposure system; pulse compression grating; spatial frequency errors; specifications

1. Introduction

Ultra-high-intensity, ultra-short-pulse lasers have significantly advanced the development of inertial fusion[1], miniature compact free electron lasers (FELs)[2] and fundamental ultra-high-intensity interactions[3]. The pulse compression grating (PCG) plays a key role in the performance of the ultra-high-intensity ultra-short laser system, which in turn has pushed PCGs toward their limits in terms of size, optical performance and resistance to laser damage[4–6]. Over the last three decades, as the peak power of high-power lasers has increased from several megawatts

(MW) to 10 petawatts (PW)[7–10], the grating dimension has also been enlarging. These laser systems today use meter-scale gratings to compress the final amplified chirped pulse.

However, with the proposal and construction of the 100 PW class or even higher power laser systems[11], the size limitation of the grating has been the bottleneck. Manufacturing techniques for large-aperture diffraction gratings[12] historically began with mechanical ruling, which was later accompanied by mainstream two-beam interference lithography (often simply cited as holography) and other representative techniques, for example, scanning beam interference lithography (SBIL)[13,14], holographic phase aperture synthesis, grating stitching[15,16]. Ruling gratings suffer from expensive production and duplication costs and greater stray light levels than holographic gratings[17], so they have been gradually replaced by the latter. At present, the world's largest two-beam laser interference lithography

Correspondence to: Chaoyang Wei, Songlin Wan, and Jianda Shao, Shanghai Institute of Optics and Fine Mechanics, Chinese Academy of Sciences, Shanghai 201800, China. Emails: siomwei@siom.ac.cn (C. Wei); songlin_wan@siom.ac.cn (S. Wan); jdshao@siom.ac.cn (J. Shao)

1

station has been developed by Lawrence Livermore National Laboratory (LLNL), which utilizes 1.1 m diameter collimating lenses[18]. Considering the homogeneity of large-aperture transmission optical material, it is difficult to further improve the aperture of the lens. To break through this limitation, SBIL was proposed by the Massachusetts Institute of Technology (MIT) and Plymouth Grating Laboratory (PGL) research team, which uses small diameter beams (about 1 or 2 mm) to generate interference fringes and expose the interference image in the photoresist on the substrate[19]. The performance of the grating fabricated by this technology is ultimately dependent on the accuracy control of the relative position between the substrate and the scanning beam. In particular, it becomes more challenging to maintain uniformity and consistency across a large area when scaling up to fabricate large-size gratings. The scanning process is time-consuming, and specialized equipment such as high-precision stages, complex optics and precise control systems are required. The complexity and cost of this equipment will also become limiting factors. Another method is stitching, which is mainly divided into exposure stitching by synthesis of multiple holographic phase sub-apertures represented by the Leningrad Nuclear Physics Institute (LNPI)[20] and mechanical stitching (multiple small gratings are stitched into large gratings) proposed by the University of Rochester[21]. For this technique, the stitching errors caused by control accuracy need to be significantly strictly limited, otherwise the far-field focus may deteriorate. However, these researches transfer the difficulty of optical manufacturing to the accuracy of control systems. As a result, with the increase of grating dimensions, today's control systems for the manufacture of state-of-the-art diffraction gratings have become extremely complex.

Therefore, the reflection exposure method has the potential to overcome some of the challenges faced in fabricating large-size gratings. By utilizing this method, issues related to optical materials, stitching and scanning methods can be eliminated. However, the focus then shifts to the fabrication of the mirror, which becomes the key difficulty in this approach. Achieving high-quality and uniform mirrors at a large scale is a challenging task. In order to evaluate the performance of the mirror, the specifications must be established to meet the needs of uniformity of the light field. For example, in the National Ignition Facility (NIF), because imperfections in the optical components can lead to problems at certain spatial frequencies, such as scattering and beam divergence as well as intensity modulations that undergo nonlinear gain, the low/mid/high spatial frequency (LSF/MSF/HSF) specification of the optics played a critical role in feedback in the polishing process to improve the quality of the optical components[22]. Similarly, to achieve high brightness of the third- and fourth-generation synchrotron/FEL light sources, it is necessary to characterize the optical surface figure, slope errors and roughness on X-ray optics over spatial frequencies as short as 0.1 mm and with slope errors reaching less than 100 nrad root mean square (RMS) or surface figure errors close to 1 nm[23]. For reflective two-beam laser static interference lithography, there is still no precedent of successfully fabricating gratings by the reflection exposure method due to the lack of scientific technology. Different from traditional focusing optical systems (e.g., inertial confinement fusion, shortwave focusing) the interference lithography system is a beam expander system, and the spatial frequency error of the reflection mirrors can affect the nonuniformity of the exposure light field for varying degrees and further determine the grating quality, but the lack of scientific specification makes the manufacturing processing blind and it is difficult to meet the requirements. For advanced processing technology, the synchronous suppression of the LSF/MSF/HSF error is the key problem for complex curved surfaces. Although various polishing techniques, such as small-tool polishing[24], magnetorheological finishing (MRF)[25] and ion beam finishing (IBF)[26], have been invented, it still seems difficult to achieve efficient convergence of full spatial frequency errors. Therefore, the mechanism between exposure quality and surface error should be first studied to clarify the manufacturing difficulties and key specifications; on this basis, advanced fabrication technology needs to be further developed to achieve success in grating fabrication by the reflective exposure method.

In this paper, a multilayer dielectric diffraction grating has been successfully fabricated by the reflection exposure method. A reflective static interference exposure system was designed; the influence of the surface error on the uniformity of the light field was strictly proved and the mirror specifications were established; besides, the novel combination process technology for the exposure mirror was proposed to realize ultra-precision forming. The development gives a brand-new approach to fabricate diffraction gratings, which paves the way for the manufacture of larger gratings to support the construction of large scientific devices.

2. Reflective two-beam laser static holographic exposure for pulse compression grating fabrication

2.1. Design of the reflective two-beam static interference exposure system

According to the principle of two-beam interference in classical physical optics[27], two monochromatic plane waves with the same polarization direction and constant path difference meet, and the light intensity distribution of the composite light field after superposition is as follows:

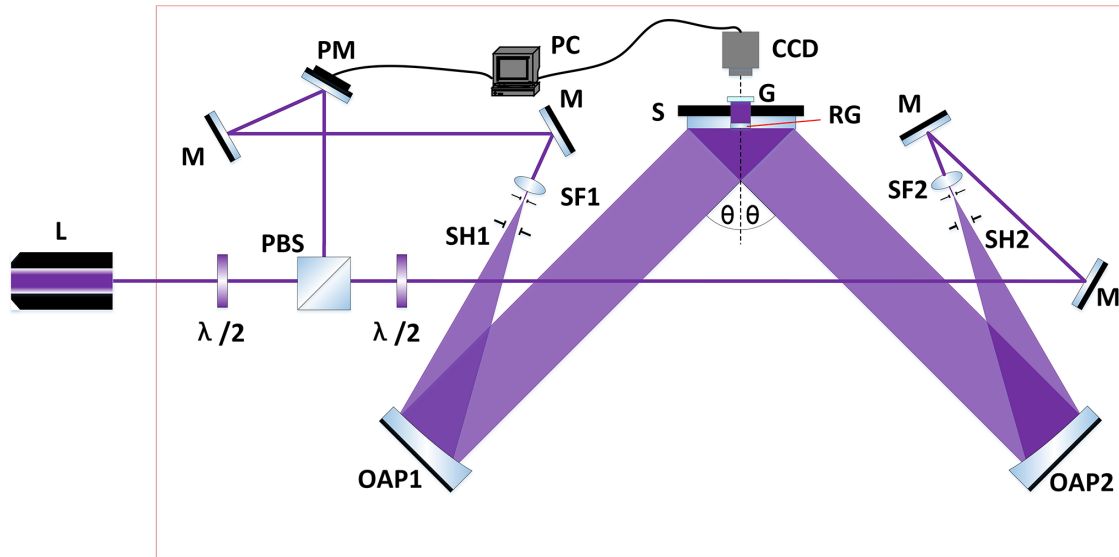$$I = I_1 + I_2 + 2\sqrt{I_1 I_2} \cos \Phi, \qquad (1)$$

Figure 1. Setup of two-beam interference lithography for MLD gratings. L, Kr$^+$ laser; M, mirror; PM, piezo mirror; $\lambda/2$, polarization rotator (e.g., half-wave plate); PBS, polarizing beam splitter; SF, spatial filter; SH, shutter; OAP, off-axis parabolic mirror; S, substrate with mount; RG, reference grating; G, ground glass.

where I_1 and I_2 are the light intensity of two beams, respectively, and their phase difference Φ can be expressed as follows:

$$\Phi(r) = k \cdot r + \Phi_0. \qquad (2)$$

Among them, $k = k_1 - k_2$ is the wave vector difference of two light waves, r is the vector path of the coherent point and Φ_0 is the initial phase difference. In general, under the condition of two-beam exposure, the wave vector of the coherent beam and the grating plane form an isosceles triangle; then $|k_1| = |k_2| = 2\pi/\lambda$. The wavelength of the exposed beam is λ, and the angle between k_1 and k_2 is 2θ; then $|k| = (4\pi/\lambda)\sin\theta$. At this time, the spatial period of the interference fringes or the spacing of the grating fringes is expressed as follows:

$$d = 2(2\pi/k) = \lambda/(2\sin\theta). \qquad (3)$$

According to the above formula, the period of the grating can be controlled by changing the angle between the two interference plane waves. The two interfering waves are usually created by division of the wavefront or amplitude in an interferometer setup. The experimental layout mainly draws inspiration from the transmission-based exposure layout used by the LLNL[28]. However, in this study, it has been modified by replacing the two exposure lenses with off-axis parabolic mirrors for reflection, as shown in Figure 1. The single longitudinal mode Kr$^+$ laser (wavelength $\lambda = 413.1$ nm) is divided by a polarizing beam splitter (PBS). By rotating the $\lambda/2$ plate, the linear polarization angle of the laser incident on the PBS is changed, and the energy distribution ratio of the two beams is changed. Another $\lambda/2$ plate is placed in one optical path behind the PBS to adjust

Table 1. The OAP mirror optical design prescription.

Optical parameter	Value	Note
Mirror diameter	300 mm	
Material	Glass ceramics	
Vertex radius of curvature	3000 mm	
Off-axis distance	240 mm	Distance from the parent vertex
Conic constant	−1	Parabola
Aspheric departure	24 μm	Astigmatic peak-to-valley departure
Measurement method	Null test with standard plane mirror	

the polarization direction of the two beams to the same angle, and then a spatial filter is placed in each arm to filter the beam. The spatial filter is composed of a micro objective lens and a pinhole, which is placed at the focal point of the off-axis parabolic (OAP) mirror to form the off-axis reflection beam expanding system, so that two plane waves are projected onto the grating substrate surface coated with photoresist to form interference fringes, and the grating mask is made. The optical parameters of the OAP mirror are shown in Table 1. Before exposure, the fringe spacing can be precisely controlled by adjusting the half angle between the mirrors.

In addition, in order to overcome the influence of the environment and ensure the stability of the interference fringes, a phase locking system composed of a piezo mirror and a fringe monitoring system is introduced to control the absolute phase difference between the two arms. The fringe monitoring system consists of a reference grating and a charge-coupled device (CCD). The grating period of the reference grating is half of that of the grating to be fabricated,

Figure 2. Reflective two-beam laser static interference lithography station for MLD grating fabrication.

which is installed at the coplanar position with the grating substrate. In this way, the first-order diffraction beams of two beams incident on the reference grating will coincide to form an interference, and the fringes are recorded by the CCD. At this time, the phase of the interference fringes of the reference grating is only related to the phase of the exposure fringes, so as to realize the fringes locking.

2.2. Manufacturing method of the MLD grating

A multilayer dielectric (MLD) structure consisting of HfO_2 with a high refractive index and SiO_2 with a low refractive index was deposited on the surface of a fused silica substrate with a size of 200 mm × 150 mm. A single SiO_2 layer with high laser damage threshold was selected as the grating etching layer. The photoresist (~500 nm) was coated on the surface of the substrate by the rotary coating process, and the photoresist was more closely combined with the substrate by baking. The grating pattern was exposed into the photoresist layer using reflective two-beam laser static interference lithography station, shown in Figure 2, utilizing 300 mm diameter OAP mirrors and a 413 nm Kr-ion laser light.
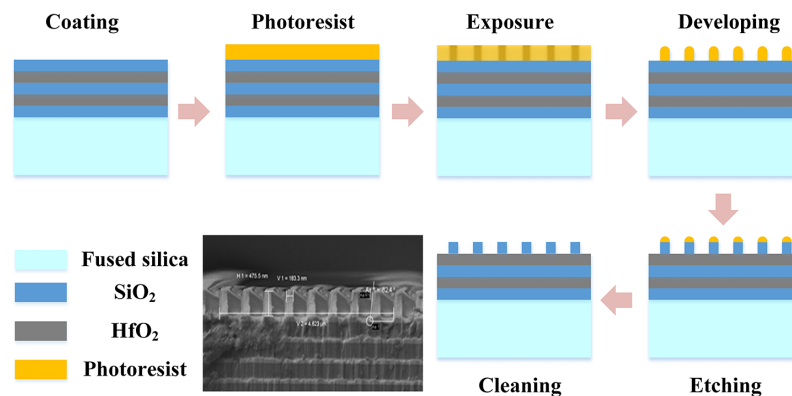
After development, the grating lines of the photoresist were examined at several positions by atomic force microscopy (AFM) to realize the uniformity monitoring of the exposure/development process. Baking hardens the mask to suit the ion beam etching, and introduces the photoresist ashing process to remove the residual glue. The mask structure was transferred by an ion beam etching machine, MRIBE-300M of the Veeco company. After etching, the remaining photoresist mask was removed by the chemical method to complete the fabrication of the grating, as shown in Figure 3.

3. Specifications and control of the spatial frequency errors of components in two-beam laser static holographic exposure

3.1. Establishment of the exposure mirror specification for the reflection exposure system

The nonuniformity of the light field intensity modulated by the figure error of the exposure mirror is the main bottleneck restricting the quality of the grating fabricated by the reflection exposure method; an insufficient surface error can affect the grating groove shape and continuity, which deteriorates the diffraction wavefront and efficiency. In order to guide the surface finishing technology of the exposure mirror, the influence of the figure error on the light field nonuniformity must be clarified, and the exposure mirror specification for the reflection exposure system should be established.

Generally, it is considered that the manufacturing difficulty of reflective mirrors is higher than that of transmission optics, because for the reflective mirrors the wavefront error is twice the figure error, while for the transmission optics, it is about 0.5 times. Therefore, for the light intensity modulation caused by the figure error, the reflection is about four times that of the transmission, which can be expressed as follows:

Figure 3. Processing steps of manufacturing MLD grating.

reflection : $U_0 = A \cdot e^{i \cdot \frac{2\pi}{\lambda} \cdot 2W_0}$,

transmission : $U_0 = A \cdot e^{i \cdot \frac{2\pi}{\lambda} \cdot (n-1) \cdot W_0}$, $\qquad$ (4)

where U_0 is the input wave function, λ is the wavelength, A is the amplitude of the light field, W_0 is the figure error distribution and n is the refractive index of the transmission optics, with the average value of 1.5.

According to the angular spectrum diffraction theory[29], the light field distribution after the propagating z unit distance (U_z) can be expressed as follows:

$$U_z = \mathcal{F}^{-1}\left(\mathcal{F}(U_0) \cdot \exp\left(i \cdot \frac{2\pi}{\lambda} \cdot z \cdot \sqrt{1 - (\lambda f_x)^2 - (\lambda f_y)^2} \right) \right),$$
$$(5)$$

where $\mathcal{F}$ is the symbol for the Fourier transform and f_x and f_y represent the horizontal and vertical frequency components in the frequency domain, respectively.

In order to directly find out the influence mechanism of the figure error on the uniformity of the light field, we convert the complex number in the formula to a real number. Furthermore, in the laser holographic exposure system, the figure error of the mirror is generally much smaller than the laser wavelength; therefore, the input wave function of the reflection exposure mirror can be further simplified by the Taylor formula:

$$U_0 \approx A \cdot \left(1 + i \cdot \frac{4\pi}{\lambda} \cdot W_0 \right). \qquad (6)$$

The Fourier transform of the input wave function is represented as the form of the impulse function, and then the light field can be expressed as follows:

set $\Phi(f_x, f_y; z) = \frac{2\pi}{\lambda} \cdot z \cdot \left(\sqrt{1 - (\lambda f_x)^2 - (\lambda f_y)^2} - 1 \right)$

$\qquad \approx -\pi\lambda \cdot z \cdot (f_x^2 + f_y^2)$,

$U_z = A \cdot \mathcal{F}^{-1}\Bigg(\Big(\delta(f_x, f_y) + \int\limits_{-\infty}^{\infty}\int\limits_{-\infty}^{\infty} \frac{i \cdot 4\pi \cdot \mathcal{F}_{W_0}}{\lambda}$

$\quad \cdot \delta(f_x - a, f_y - b)\, da\, db \Big) \cdot e^{i \cdot \left(\Phi + \frac{2\pi z}{\lambda} \right)} \Bigg)$

$= \frac{A \cdot e^{i \cdot \frac{2\pi z}{\lambda}}}{2\pi} \iint \Bigg(\delta(f_x, f_y) + i \cdot \frac{4\pi}{\lambda} \cdot \int\limits_{-\infty}^{\infty}\int\limits_{-\infty}^{\infty} \mathcal{F}_{W_0} e^{i\Phi}$

$\quad \cdot \delta(f_x - a, f_y - b) \cdot da\, db \Bigg) \cdot e^{i \cdot 2\pi(f_x x + f_y y)}\, df_x\, df_y, \qquad (7)$

where $\delta(f_x, f_y)$ is the impulse function, $\mathcal{F}_{W_0}$ represents the Fourier transform of the figure error W_0 and a, b are the intermediate variables to rewrite the formula by impulse function convolution.

Furthermore, the figure error distribution W_0 is always a real function; therefore, Equation (7) can be further simplified as follows:

from $\mathcal{F}_{W_0}(f_x, f_y) = \mathcal{F}_{W_{0*}}(-f_x, -f_y)$ for real W_0 :

set $\mathcal{F}_{W_0}(f_x, f_y) = r(f_x, f_y) \cdot e^{i \cdot \theta(f_x, f_y)}$,

$U_z = \cdot e^{i \cdot \frac{2\pi z}{\lambda}} \cdot \Bigg(1 + \frac{1}{2\pi} \int\limits_{-\infty}^{\infty}\int\limits_{0}^{\infty} i \cdot \frac{4\pi}{\lambda} r(a,b)\, e^{i \cdot \Phi(a,b;z)}$

$\quad \cdot \left(e^{i \cdot (2\pi(ax+by) + \theta(a,b))} + e^{-i \cdot (2\pi(ax+by) + \theta(a,b))} \right) \cdot da\, db \Bigg)$

$= A \cdot e^{i \cdot \frac{2\pi z}{\lambda}} \cdot \Bigg(1 + \frac{1}{2\pi} \int\limits_{-\infty}^{\infty}\int\limits_{0}^{\infty} \frac{8\pi}{\lambda} \cdot r(a,b) \cdot e^{i\left(\Phi(a,b;z) + \frac{\pi}{2} \right)}$

$\quad \cdot \cos(2\pi(ax+by) + \theta(a,b)) \cdot da\, db \Bigg), \qquad (8)$

where $r(f_x, f_y)$ and $\theta(f_x, f_y)$ are the module and the argument of the Fourier transform of W_0, respectively.

The distribution of the light intensity is the modulus of U_z, and considering that the figure error of the exposure mirror is much smaller than half of the wavelength, it can be further expressed as follows:

$\|U_z\| = \sqrt{U_z \cdot U_z^*}$

$= A \cdot \Bigg(1 - 4 \cdot \int\limits_{-\infty}^{\infty}\int\limits_{0}^{\infty} \frac{2}{\lambda} \cdot r(a,b) \cdot \sin(\Phi(a,b;z))$

$\quad \cdot \cos(2\pi(ax+by) + \theta(a,b)) da\, db$

$\quad + 4 \cdot \int\limits_{-\infty}^{\infty}\int\limits_{0}^{\infty} \left(\frac{2}{\lambda} \cdot r(a,b) \right)^2 \cdot \cos^2(2\pi(ax+by) + \theta(a,b)) \cdot da\, db \Bigg)^{-\frac{1}{2}}$

when $r(a,b) \ll \frac{\lambda}{2}$

$\approx A \cdot \Bigg(1 - \frac{1}{2\pi} \int\limits_{-\infty}^{\infty}\int\limits_{0}^{\infty} \frac{16\pi}{\lambda} \cdot r(a,b) \cdot \sin(\Phi(a,b;z))$

$\quad \cdot \cos(2\pi(ax+by) + \theta(a,b)) da\, db \Bigg)^{-\frac{1}{2}}$

$\approx A \cdot \left(1 - \mathcal{F}^{-1}\left(\mathcal{F}\left(\frac{4\pi W_0}{\lambda} \right) \cdot \sin(\Phi(f_x, f_y; z)) \right) \right). \qquad (9)$

It is interesting to find that the diffraction law of the light field in the exposure system can be simplified as a filter of the sine function, as shown in Figure 4.

The proposed model successfully reveals the quantitative evolution law of light field nonuniformity affected by the figure error of the mirrors in the exposure system. Different from the traditional understanding that the periodic figure error is prohibited due to the Talbot effect, the full spatial frequency errors are all needed to be strictly constrained. Essentially, the Talbot effect is a special case of the proposed model, where the detailed derivations are shown below:
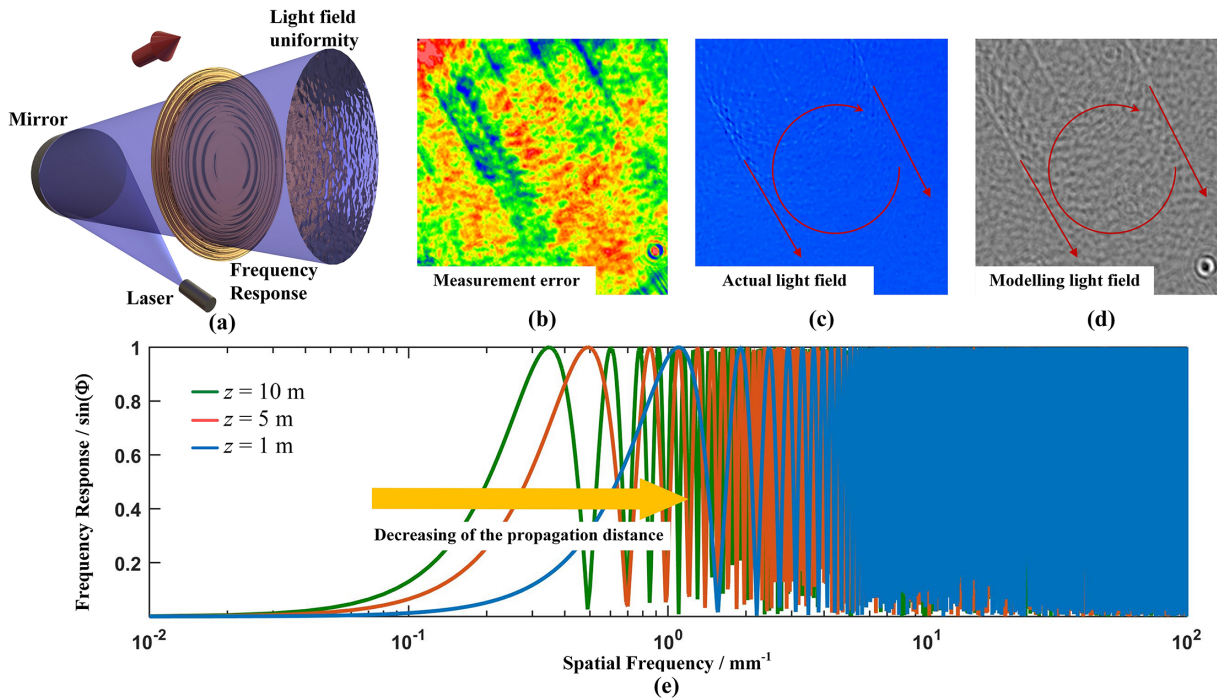
Figure 4. (a) Schematic diagram of the light field diffraction law in the exposure system. (b) Local figure error example with MSF and HSF errors. (c) Actual light field photo caused by the example surface. (d) Theoretical prediction result calculated by the proposed model. (e) Sine filter characteristic of the light field diffraction law.

for periodic figure error $W_0 = A_{\text{wave}} \sin\left(\frac{2\pi}{\Lambda} \cdot x\right)$,

$$\frac{\|U_z\|}{A} \approx 1 - \frac{4\pi A_{\text{wave}}}{\lambda} \cdot \mathcal{F}^{-1}\left(\mathcal{F}\left(\sin\left(\frac{2\pi}{\Lambda} \cdot x\right)\right) \cdot \sin\left(\Phi\left(f_x, f_y; z\right)\right)\right)$$

$$= 1 - \frac{4\pi A_{\text{wave}}}{\lambda} \cdot \mathcal{F}^{-1}\left(\delta\left(f_x \pm \frac{1}{\Lambda}, f_y\right) \cdot \sin\left(\Phi\left(f_x, f_y; z\right)\right)\right)$$

$$= 1 - \underbrace{\sin\left(-\pi\lambda \cdot z \cdot \frac{1}{\Lambda^2}\right)}_{\text{Talbot modulation}} \cdot \frac{4\pi A_{\text{wave}}}{\lambda} \cdot \sin\left(\frac{2\pi}{\Lambda} \cdot x\right),$$

$$\tag{10}$$

where Λ is the period of the figure error and A is the amplitude of the light field.

The spectrum of the periodic figure error is an impulse function, the light field distribution of the periodic figure error is still periodic and the amplitude changes periodically with the propagation distance z. The Talbot distance period z is $2\Lambda^2/\lambda$, which is consistent with the Talbot theory.

Obviously, based on the above quantitative evolution law, we can establish a general standard to judge whether the mirror specifications of the exposure system meet the requirements. Since the optical specifications of the mirrors are largely based on the results of propagation modeling described above, modeling of the light field and the optical specifications are closely tied and should be consistent with one another. In both modeling and specifications,

we differentiate between spatial frequency regions, since each involves different light field performance issues. In order to cover these frequency bands, it is also necessary to consider the frequency band range of different measuring instruments.

To deal with these issues, we break the spatial frequency regime into three regions, namely the LSF/MSF/HSF specification of the optics. Considering the unique shape of the sine filter, the light field is insensitive to the LSF error since sine filter tends to 0 in the LSF region, and the Talbot effect appears stable in the MSF band because it is less affected by the perturbation of the propagation distance. Therefore, we use the first period of the sine function as the boundary to divide the MSF and HSF errors, and the boundary between the LSF and MSF errors is defined, which follows the –10 dB formula[30] and also facilitates the field of view connection of the measuring instruments. The spatial frequency error higher than $1/\lambda$ is the evanescent wave, which should be excluded from the frequency range. The frequency error division scheme applicable to the grating exposure system is shown below.

In the proposed frequency error division specification, the LSF error mainly affects the straightness of the grating line, where the light field uniformity is insensitive to the LSF error. According to previous research[31], to ensure the diffracted wavefront for the grating of $\lambda/2$ PV or even better, the LSF error of the exposure mirror should be as low as $\lambda/10$ PV.

Table 2. Exposure mirror specifications for the reflection exposure system.

Specification	Spatial frequency range	Index requirements
LSF error	$f < 1/\sqrt{30\lambda z}$	PV < 60 nm[31]
MSF error	$1/\sqrt{30\lambda z} \leq f < 1.414/\sqrt{\lambda z}$	RMS $< \lambda/640$ (0.65 nm for $\lambda = 413.1$ nm)
HSF error	$1.414/\sqrt{\lambda z} \leq f < 1/\lambda$	RMS $< \lambda/820$ (0.5 nm for $\lambda = 413.1$ nm)
Others	PSD curve of figure error has no peaks in either direction	

Note: λ is the working wavelength of exposure system; z is the propagation distance.

The MSF and HSF errors, which we named MHSF errors, are the main factor to deteriorate the light field uniformity. Errors with frequency greater than f_1 can all be mapped into the exposure light field distribution. Therefore, the MHSF errors in each sub-aperture of the exposure mirror should be controlled.

To ensure the nonuniformity of the light field meets the requirement of the exposure system, we limit the nonuniformity of the light field below the nonuniformity of the light source as the basis. Considering the light field nonuniformity of the common exposure light source is around $\pm5\%$, combined with Plancherel's theorem and the three-sigma rule[30], the exposure mirror specifications can be established to ensure that the light field does not deteriorate.

The exposure mirror specifications listed in Equation (11) constrain both MSF and HSF errors for the whole surface; besides, to ensure MHSF error distribution consistency, random sampling measurements in multiple positions should be done to avoid the local unsatisfied region:

$$\frac{4\pi}{\lambda} \cdot 3 \cdot \text{RMS}\left(\mathcal{F}(\text{err}_{\text{MHSF}}) \cdot \sin\left(\Phi\left(f_r\right)\right)\right) < 5\%$$

$$\text{with } f_r = \sqrt{f_x^2 + f_y^2} \in \left(\frac{1}{\sqrt{30\lambda z}}, \frac{1}{\lambda}\right)$$

$$\Rightarrow \frac{12\pi}{\lambda} \cdot \sqrt{\text{RMS}^2(\text{err}_{\text{MHSF}}) \cdot \frac{1}{2\pi}\int_{-\pi}^{\pi}\sin^2(\Phi)\,\mathrm{d}\Phi} < 5\%$$

$$\Rightarrow \text{RMS}^2(\text{err}_{\text{MHSF}}) < \lambda/533, \quad \frac{1}{\sqrt{30\lambda z}} < f < \frac{1}{\lambda}. \quad (11)$$

The laser wavelength used in our exposure system is 413.1 nm; therefore, the RMS of the MHSF error distribution RMS(err$_{\text{MHSF}}$) in each region should be controlled to be lower than 0.77 nm. In addition, since the existence of the Talbot effect can reprint the periodic light field nonuniformity distribution similar to the grating structure, we have added the power spectral density (PSD) curve constraint to avoid the periodic structure in the figure error.

The results of the MSF and HSF errors mentioned in Equation (11) are mixed together, which is not convenient for the judgment of practical measurement results. We decompose each spatial frequency error specification of the exposure mirror, as shown in Table 2.

It can be seen that the difficulty of the fabrication also depends on the propagation distance of the exposure system, according to Figure 5. Therefore, the difficulty of the fabrication will increase with the increase of the propagation distance, because more LSF errors are introduced by the change of the filter. Therefore, the optical path length of the exposure system is designed to be more compact, where the propagation distance in our experiment is shortened to be 3.3 m. Hereafter, the MHSF region is varied from 0.156 to 2.42×10^3 mm^{-1}, which reduces the
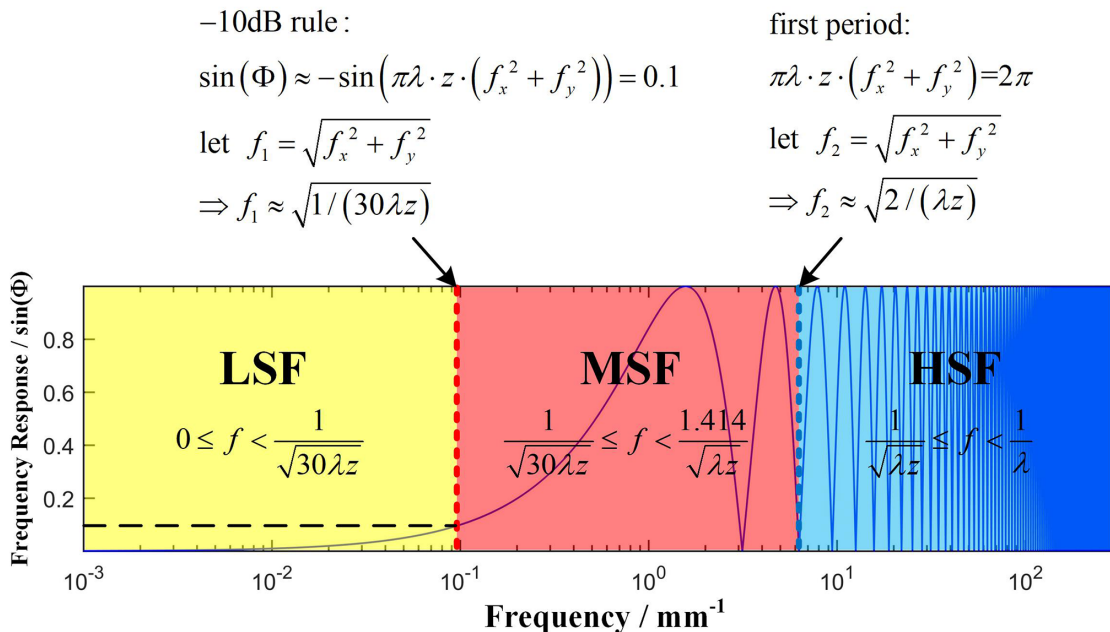

−10dB rule :
$$\sin(\Phi) \approx -\sin\left(\pi\lambda \cdot z \cdot \left(f_x^2 + f_y^2\right)\right) = 0.1$$
let $f_1 = \sqrt{f_x^2 + f_y^2}$
$$\Rightarrow f_1 \approx \sqrt{1/(30\lambda z)}$$

first period:
$$\pi\lambda \cdot z \cdot \left(f_x^2 + f_y^2\right) = 2\pi$$
let $f_2 = \sqrt{f_x^2 + f_y^2}$
$$\Rightarrow f_2 \approx \sqrt{2/(\lambda z)}$$

Figure 5. The frequency error division scheme for the grating exposure system.
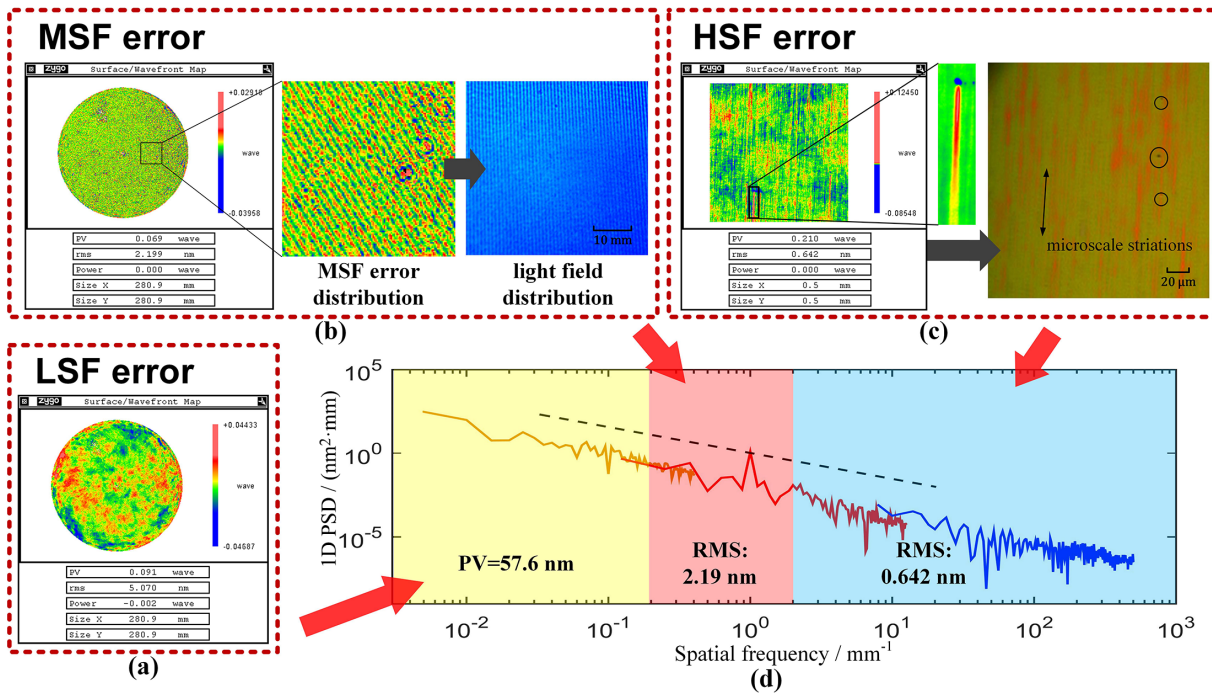
Figure 6. Surface shape error distribution of the off-axis parabolic mirror under the traditional polishing process. (a) The figure error of the off-axis mirror measured by using a 4″ Zygo interferometer. (b) The MSF error filtered according to the model specification and a photo of the light field distribution. (c) The HSF error measured by a Zygo white light profiler with a 20 × lens and a photo of the microscale grating mask. (d) 1D-PSD curves.

difficulty of the fabrication process. Hereafter, we combined the experimental results to verify that the main factor affecting the nonuniformity of light field intensity is the MHSF error.

3.2. Processing technology and results for the exposure mirrors

Based on the exposure mirror specifications shown above, it is not easy to fabricate a satisfactory mirror by the traditional deterministic optical processing technologies; a complex curved mirror cannot be fabricated by the full-aperture processing method, but the MHSF error is easy to introduce during sub-aperture grinding and polishing process (e.g., MRF, computer-controlled optical surfacing (CCOS) and IBF), such as the tool trace and surface micro plough on the processed optical surface. At present, magnetorheological polishing technology is an effective means to realize high-efficiency and high-precision machining of components. However, for the traditional orthogonal MRF processing method, the periodic MSF error is difficult to eliminate. After the mirror (93% effective aperture) is polished by MRF, although the RMS of the low-frequency profile converges to 5.07 nm rapidly, there is obvious periodic MSF error distribution, as shown in Figures 6(a) and 6(b). It can be found that the figure error reaches a high precision, but the RMS of the MSF error has already exceeded the proposed specification.

The light field distribution is in the shape of MSF error, which is consistent with the theoretical prediction, as shown in Figure 6(b). Besides, the PSD function specification is used to judge whether there is periodic structure[32]. The calculated results are shown in Figure 6(d). It can be seen that the PSD curve has an obvious peak at the period of 1 mm, which is consistent with the processing step of the MRF, indicating that the traditional processing raster path of the MRF is the main reason for the MSF error and it cannot be used in the exposure system.

Besides, the HSF error is also a crucial source to affect the light field uniformity, especially the marks in the micrometer scale. Firstly, the MRF tool can introduce the microscale 'regular striations' along the rotation direction of the magneto-rheological (MR) wheel; secondly, the mismatch between the tool and asphere and the slurry agglomeration can introduce randomized marks on the polishing surface. We observe the influence of the HSF error on the mask quality using an optical microscope (magnified 200 times), as shown in Figure 6(c).

The microscale 'regular striations' can be reflected in the grating mask, which means the existence of nonuniform light field distribution. The microscale 'regular striations' are formed during the shear removal process of the MRF polishing powder, where scattered plastic deformation occurs. Although the 'regular striations' only exist in a few regions (Figure 6(c)), the RMS in the small area can be enlarged up to 3 nm, as shown in Figure 6(c). The photo of the microscale grating mask also shows significant similar striations.

Figure 7. (a) MRF and "magic" angle step technology. (b) Small tool processing and smooth pseudorandom path.
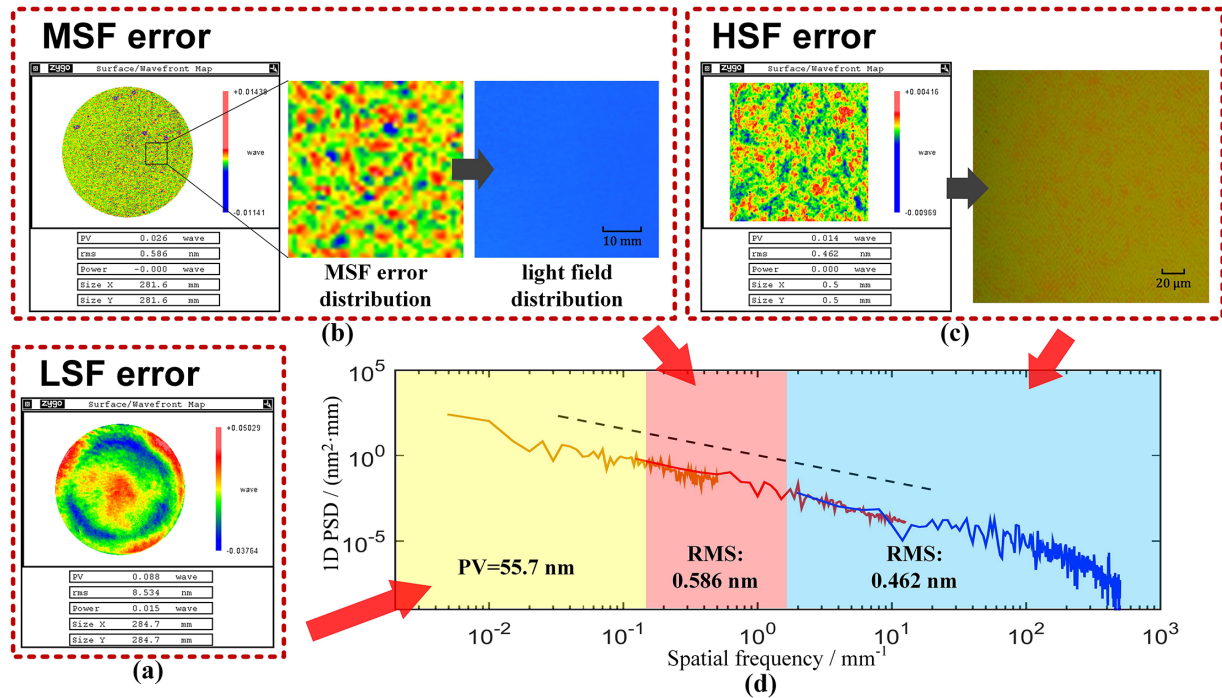

Figure 8. Surface shape error distribution of the off-axis parabolic mirror after the combined polishing process. (a) Using a 4" Zygo interferometer to measure the figure error of the off-axis mirror. (b) The MSF error filtered according to the model specification and a photo of the light field distribution; (c) The HSF error measured by a Zygo white light profiler with a 20 × lens and a photo of the microscale grating mask. (d) 1D-PSD curves.

The results indicate that all 'regular striations' at the micrometer level should be prohibited, which makes the polishing process significantly more difficult.

To fabricate a satisfactory mirror without the above errors, we introduced a series of self-developed novel processing technologies. To suppress the MHSF error introduced by the MRF tool, we utilized the 'magic' angle step state of the MRF[33], which involves specific path angles and steps with a bandwidth of only tens of micrometers (the 'magic' angle step). This state allows for the stable realization of a surface error convergence without significant path ripple. The schematic diagram is shown in Figure 7(a); besides, the composition ratio of the MR fluid and the flow rate/viscosity of the MR wheel have been optimized to reduce the 'regular striation' depth. To overcome the defects produced by the small tool, we introduced a smooth pseudo-random path[34]

to smooth the MSF error and adopted a semi-flexible pitch tool[35] to achieve a better surface quality, as shown in Figure 7(b).

Combining the proposed polishing technologies above, a novel polishing process based on the MRF and small-tool smoothing technology is formed. The figure error of the exposure mirror after polishing is shown in Figure 8(a). The MSF error filtered according to the model specification is shown in Figure 8(b), where the RMS of the MSF error is suppressed down to 0.586 nm and the periodic error is fully eliminated. Besides, the microscale sharp 'regular striations' are greatly suppressed by the developed smoothing process, and the RMS of the HSF is suppressed down to 0.462 nm. Both the MSF and HSF errors have high isotropic distributions and the PSD curves are smooth and have no peaks, as shown in Figure 8(d). The MHSF error can be
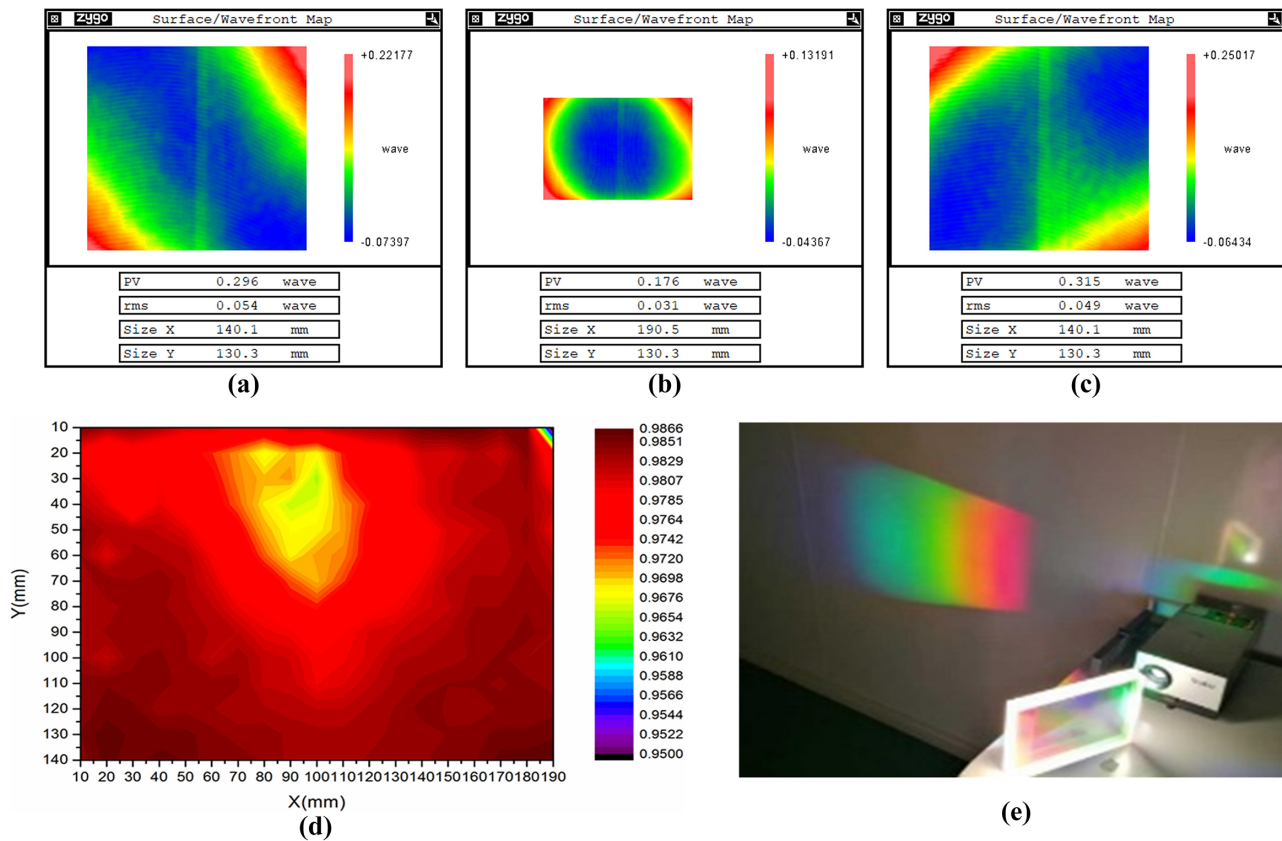
Figure 9. Diffraction wavefront and efficiency distribution of the MLD grating. (a) −1st order diffracted wavefront. (b) Zeroth order diffracted wavefront. (c) +1st order diffracted wavefront. (d) The diffraction efficiency map of the MLD grating at 1740 l/mm shows excellent uniformity of diffraction efficiency over the entire aperture for 1053 nm (Ave = 98.1%, σ = 0.3%, Max = 98.6%). (e) A 200 mm × 150 mm, 1740 l/mm MLD grating designed for use at 1053 nm, fabricated by reflective lithography.

expressed as the square average of the MSF and HSF errors; then the MHSF error is 0.746 nm, which meets the proposed specification shown in Table 2.

Furthermore, the light field distribution and the mask quality are also checked to ensure the effectiveness of the new mirror fabricated by the novel combination process, as shown in Figures 8(b) and 8(c). It is obvious that the nonuniformity has been greatly suppressed, which is highly consistent with the proposed prediction model. Hereafter, the diffraction grating can be made by the new mirrors fabricated by the proposed new processing method.

3.3. Performance of the grating fabricated by the reflection exposure method

The grating was examined by full-aperture interferometry using a Zygo 24"-aperture, phase-shifting interferometer operating at 1053 nm. Figure 9 shows the diffracted wavefront at ±1st orders and zeroth order. The overall PV of 0.315 waves is considered to be good for an MLD grating of this size and shape that has both surface figure and holographic errors.

In the laser photometry map of the grating diffraction efficiency, the average diffraction efficiency of −1st order is 98.1%, which reaches the same level of diffraction as the grating fabricated by the transmission method, as shown in Figure 9(d).

The successful grating fabrication by the reflection method proves the accessibility issue of surface manufacturing for reflection requirements, which has paved the way for future large-aperture reflection exposure systems, and related work is also being developed.

4. Conclusions

In conclusion, we have proposed and demonstrated a model to describe the phase modulations due to figure errors of the optics in the system, which are transformed into exposure optical field intensity modulation. Based on the model, the specification of the optics meeting the performance of the off-axis reflective exposure system was developed. It was found that different from the focusing optical system, the relationship between the light field and figure errors follows a sine function spatial filtering process and varies with the propagation distance. An advanced manufacturing process

to achieve controllable optical figuring and finishing of the off-axis reflective exposure mirrors was developed under the guidance of the specification. Finally, the grating fabricated by reflective two-beam laser static interference lithography can reach the same quality as that fabricated by the transmission method. We believe that the reflective exposure method opens new avenues for solving the size limitation of the PCG and can benefit high-power laser technology that relies on large gratings.

Acknowledgements

References

1. A. B. Zylstra, O. A. Hurricane, D. A. Callahan, A. L. Kritcher, J. E. Ralph, H. F. Robey, J. S. Ross, C. V. Young, K. L. Baker, D. T. Casey, T. Döppner, L. Divol, M. Hohenberger, S. Le Pape, A. Pak, P. K. Patel, R. Tommasini, S. J. Ali, P. A. Amendt, L. J. Atherton, B. Bachmann, D. Bailey, L. R. Benedetti, L. Berzak Hopkins, R. Betti, S. D. Bhandarkar, J. Biener, R. M. Bionta, N. W. Birge, E. J. Bond, D. K. Bradley, T. Braun, T. M. Briggs, M. W. Bruhn, P. M. Celliers, B. Chang, T. Chapman, H. Chen, C. Choate, A. R. Christopherson, D. S. Clark, J. W. Crippen, E. L. Dewald, T. R. Dittrich, M. J. Edwards, W. A. Farmer, J. E. Field, D. Fittinghoff, J. Frenje, J. Gaffney, M. Gatu Johnson, S. H. Glenzer, G. P. Grim, S. Haan, K. D. Hahn, G. N. Hall, B. A. Hammel, J. Harte, E. Hartouni, J. E. Heebner, V. J. Hernandez, H. Herrmann, M. C. Herrmann, D. E. Hinkel, D. D. Ho, J. P. Holder, W. W. Hsing, H. Huang, K. D. Humbird, N. Izumi, L. C. Jarrott, J. Jeet, O. Jones, G. D. Kerbel, S. M. Kerr, S. F. Khan, J. Kilkenny, Y. Kim, H. Geppert Kleinrath, V. Geppert Kleinrath, C. Kong, J. M. Koning, J. J. Kroll, M. K. G. Kruse, B. Kustowski, O. L. Landen, S. Langer, D. Larson, N. C. Lemos, J. D. Lindl, T. Ma, M. J. MacDonald, B. J. MacGowan, A. J. Mackinnon, S. A. MacLaren, A. G. MacPhee, M. M. Marinak, D. A. Mariscal, E. V. Marley, L. Masse, K. Meaney, N. B. Meezan, P. A. Michel, M. Millot, J. L. Milovich, J. D. Moody, A. S. Moore, J. W. Morton, T. Murphy, K. Newman, J. M. G. Di Nicola, A. Nikroo, R. Nora, M. V. Patel, L. J. Pelz, J. L. Peterson, Y. Ping, B. B. Pollock, M. Ratledge, N. G. Rice, H. Rinderknecht, M. Rosen, M. S. Rubery, J. D. Salmonson, J. Sater, S. Schiaffino, D. J. Schlossberg, M. B. Schneider, C. R. Schroeder, H. A. Scott, S. M. Sepke, K. Sequoia, M. W. Sherlock, S. Shin, V. A. Smalyuk, B. K. Spears, P. T. Springer, M. Stadermann, S. Stoupin, D. J. Strozzi, L. J. Suter, C. A. Thomas, R. P. J. Town, E. R. Tubman, C. Trosseille, P. L. Volegov, C. R. Weber, K. Widmann, C. Wild, C. H. Wilde, B. M. Van Wonterghem, D. T. Woods, B. N. Woodworth, M. Yamaguchi, S. T. Yang, and G. B. Zimmerman, Nature **601**, 542 (2022).
2. W. Wang, K. Feng, L. Ke, C. Yu, Y. Xu, R. Qi, Y. Chen, Z. Qin, Z. Zhang, M. Fang, J. Liu, K. Jiang, H. Wang, C. Wang, X. Yang, F. Wu, Y. Leng, J. Liu, R. Li, and Z. Xu, Nature **595**, 516 (2021).
3. T. M. Baer and N. P. Bigelow, Nature **463**, 26 (2010).
4. R. Y. Chen, Y. Z. Wang, J. D. Shao, Y. Cao, Y. H. Zhang, Z. H. Wang, Y. C. A. Shao, Y. X. Jin, K. Yi, J. B. Hu, Y. Xu, Y. X. Leng, and R. X. Li, IEEE Photonics Technol. Lett. **34**, 93 (2022).
5. W. F. Zhang, W. J. Kong, G. M. Wang, F. Xing, F. Zhang, H. N. Zhang, and S. G. Fu, Opt. Eng. **60**, 020902 (2021).
6. F. Kong, H. Huang, L. Wang, J. Shao, Y. Jin, Z. Xia, J. Chen, and L. Li, Opt. Laser Technol. **97**, 339 (2017).
7. C. N. Danson, C. Haefner, J. Bromage, T. Butcher, J. C. F. Chanteloup, E. A. Chowdhury, A. Galvanauskas, L. A. Gizzi, J. Hein, D. I. Hillier, N. W. Hopps, Y. Kato, E. A. Khazanov, R. Kodama, G. Korn, R. X. Li, Y. T. Li, J. Limpert, J. G. Ma, C. H. Nam, D. Neely, D. Papadopoulos, R. R. Penman, L. J. Qian, J. J. Rocca, A. A. Shaykin, C. W. Siders, C. Spindloe, S. Szatmari, R. Trines, J. Q. Zhu, P. Zhu, and J. D. Zuegel, High Power Laser Sci. Eng. **7**, e54 (2019).
8. W. Li, Z. Gan, L. Yu, C. Wang, Y. Liu, Z. Guo, L. Xu, M. Xu, Y. Hang, Y. Xu, J. Wang, P. Huang, H. Cao, B. Yao, X. Zhang, L. Chen, Y. Tang, S. Li, X. Liu, S. Li, M. He, D. Yin, X. Liang, Y. Leng, R. Li, and Z. Xu, Opt. Lett. **43**, 5681 (2018).
9. Z. Gan, L. Yu, S. Li, C. Wang, X. Liang, Y. Liu, W. Li, Z. Guo, Z. Fan, X. Yuan, L. Xu, Z. Liu, Y. Xu, J. Lu, H. Lu, D. Yin, Y. Leng, R. Li, and Z. Xu, Opt. Express **25**, 5169 (2017).
10. Y. Zhou, Z. Qin, X. Zhou, and G. Xie, High Power Laser Sci. Eng. **10**, e41 (2022).
11. F. Wu, J. Hu, X. Liu, Z. Zhang, P. Bai, X. Wang, Y. Zhao, X. Yang, Y. Xu, and C. Wang, High Power Laser Sci. Eng. **10**, e38 (2022).
12. N. Bonod and J. Neauport, Adv. Opt. Photonics **8**, 156 (2016).
13. G. S. Pati, R. K. Heilmann, P. T. Konkola, C. Joo, C. G. Chen, E. Murphy, and M. L. Schattenburg, J. Vacuum Sci. Technol. B **20**, 2617 (2002).
14. S. Lu, R. Cheng, K. Yang, Y. Zhu, L. Wang, and M. Zhang, Opt. Eng. **57**, 104107 (2018).
15. L. Zeng and L. Li, Opt. Lett. **31**, 152 (2006).
16. Y. Lu, X. Qi, X. Mi, S. Jiang, H. Yu, X. Li, and L. Yin, Acta Opt. Sin. **36**, 0505001 (2016).
17. N. K. Pavlycheva, J. Opt. Technol. **89**, 142 (2022).
18. H. T. Nguyen, J. A. Britten, T. C. Carlson, J. D. Nissen, L. J. Summers, C. R. Hoaglan, M. D. Aasen, J. E. Peterson, and I. Jovanovic, Proc. SPIE **5991**, 59911M (2006).
19. Y. Zhao, "Ultra-high precision scanning beam interference lithography and its application : spatial frequency multiplication," PhD. Thesis (Massachusetts Institute of Technology, 2008).
20. B. G. Turukhano, V. P. Gorelik, S. N. Kovalenko, and N. Turukhano, Opt. Laser Technol. **28**, 263 (1996).
21. J. Qiao, A. Kalb, M. J. Guardalben, G. King, D. Canning, and J. H. Kelly, Opt. Express **15**, 9562 (2007).
22. P. A. Baisden, L. J. Atherton, R. A. Hawley, T. A. Land, J. A. Menapace, P. E. Miller, M. J. Runkel, M. L. Spaeth, C. J. Stolz, T. I. Suratwala, P. J. Wegner, and L. L. Wong, Fusion Sci. Technol. **69**, 295 (2016).
23. H. Wang, S. Moriconi, and K. Sawhney, Light Sci. Appl. **10**, 195 (2021).

24. S. Wan, C. Wei, C. Hu, H. Gu, and J. Shao, Opt. Express **29**, 23582 (2021).
25. W.-L. Zhu and A. Beaucamp, Int. J. Mach. Tools Manufact. **158**, 103634 (2020).
26. Z. Zhang, J. Yan, and T. Kuriyagawa, Int. J. Extreme Manufact. **1**, 022001 (2019).
27. M. Born and E. Wolf, *Principles of Optics: Electromagnetic Theory of Propagation, Interference and Diffraction of Light* (Cambridge University Press, Cambridge, 1964).
28. R. D. Boyd, J. A. Britten, D. E. Decker, B. W. Shore, and L. Li, Appl. Opt. **34**, 1697 (1995).
29. K. Iizuka and I. Keigo, *Engineering Optics* (Springer, New York, 2008), Vol. 35.
30. P. Diniz, S. Netto, and E. D. Silva, *Digital Signal Processing: System Analysis and Design* (Cambridge University Press, Cambridge, 2010).
31. F. Koch, D. Lehr, and T. Glaser, Proc. SPIE **10448**, 104481L (2017).
32. M. L. Spaeth, K. R. Manes, C. C. Widmayer, W. H. Williams, P. K. Whitman, M. A. Henesian, I. F. Stowers, and J. Honig, Opt. Eng. **43**, 2854 (2004).
33. S. Wan, C. Wei, C. Hu, G. Situ, and J. Shao, Int. J. Mach. Tools Manufact. **161**, 103673 (2021).
34. H. J. Li, X. Y. Li, S. L. Wan, C. Y. Wei, and J. D. Shao, Appl. Opt. **60**, 7732 (2021).
35. X. Li, C. Wei, S. Zhang, W. Xu, and J. Shao, Appl. Opt. **58**, 4406 (2019).